Interaction between Two Jets Exhausted from Nozzles Arranged in Parallel

by

Natsuo HATTA*, Hitoshi FUJIMOTO* and Jun-ichi KOKADO**
(Received September 7, 1990)

Abstract

This paper describes flow structures of two interacting free jets expanded from uniform sonic nozzles into a stagnant ambient gas region. The Euler equations are numerically solved using a TVD (Total Variation Diminishing) scheme developed by Chakravarthy and Osher. First, a choked underexpanded supersonic single free jet is investigated in detail in the context of continuum ideal gas dynamics. By comparing the numerical results so obtained with the experimental ones it is confirmed that the present scheme is reliable. Second, the effect of the distance between the nozzle centerlines on the flow field of the two jets interacting with each other is examined from an analytical standpoint. Thereby, we find that a perfectly time-converged numerical solution is not reached at all, even at $t \to \infty$ (t: time). Rather, the solution may be regarded as quasi-steady or slightly oscillatory. Characteristic shock systems, density and pressure distributions of the interacting two free jets are quantitatively discussed in view of the numerical experiments. Also, a few fresh findings are described.

1. Introduction

Single-phase or multiphase free jets are of great technical importance for various engineering applications. Therefore, we have investigated a numerical analysis of the gas-particle mixture flows and nearly established a theoretical or analytical procedure to evaluate all of the flow properties for both gas and particle phases through a nozzle[1]~[3]. Subsequently, the numercal analysis of gas-particle mixture flows not only in a nozzle but also in a free jet region has been performed by incorporating the particle trajectory method into a system of gas-phase equations in the so-called two-fluid model[4]. Our essential purpose of such investigations is to find the theoretical heat transfer mechanism of the mist or spray cooling, which is applied to the secondary cooling zone of continuously cast slabs. In this sense, we have investigated the numerical analysis of the flow pattern of gas and particle phases impinging upon a solid wall, and thereby examined the effect of the particle size on the flow field[5].

* Department of Mineral Science & Technology, Faculty of Eng., Kyoto Univ., Kyoto 606
** Emeritus professor (Kyoto Univ.)

Now, for a relatively gentle cooling of slabs, the cooling intensity is virtually required to be uniform widthwise. Hence, the interference of two jets adjacent to each other can give rise to trouble in achieving the uniformity of water spray volume distribution. According to some previous studies[6]~[9], when the gas flow fluctuates, the particles smaller than 2 μm or so in diameter follow the fluctuation. The fluctuation of the particle motion becomes smaller for the larger particles. In this sense, the effect of the interaction of two single-phase free jets as well as two gas-particle free jets in a parallel arrangement should be investigated from an analytical point of view.

This paper is concerned with structures of interacting single-phase free jets expanded from two parallel sonic nozzles into a stagnant ambient gas region. The present simulations are performed by the two-dimensional Cartesian coordinate system. Here, we wish to note that there are some experimental investigations on interacting single-phase free jets. For example, we have recently seen a few works treating structures of interacting free jets from two sonic nozzles for various angles between nozzle centerlines (45~180 degrees)[10]~[12]. However, it does not seem that the problem of the interaction between two parallel jet flows has been treated.

It is commonly accepted that a single supersonic free jet forms the so-called shock cell structure and it is characterized by the ratio of the jet gas pressure at the nozzle exit to the ambient gas pressure. However, structures of interacting free jets are strongly dependent upon the distance between the centerlines of nozzles in a parallel arrangement. Here, two cases are analyzed where the distance is fixed at $2\bar{H}$ and $3\bar{H}$. ($\bar{H}$ denotes the height of the rectangular nozzle section with $\bar{H}$ high and $\bar{W}$ wide at the nozzle exit.)

When the distance between the centerlines of two nozzles is taken to be relatively large, two jet flows are almost independent of each other. Therefore, the first shock cell structure appears to be very similar to the single free jet case. Again, the existence of the barrel shock is appreciably distinctly recognized even in the interference side along the first shock cell boundaries of the two jets. However, in the case where the distance is taken at $3\bar{H}$, the two second shock cells are observed to interact with each other, and the whole height of the interacting jets tends to shrink in the downstream region of the first shock cells. In addition, the point where the gas stagnates exists on the symmetric axis (plane) between the two jets, and there is a reverse flow upstream from the aforementioned stagnation point. Also, two circulating flows can be observed in a relatively wide range between the first shock cells.

When the distance between the centerlines of the two jets is taken to be small, the configuration of the first shock cell structures is different from that of the single free jet. The point where the two jets interact with each other approaches a considerably

upstream side along the symmetric axis (plane) compared with the case of the large nozzle distance. Also the barrel shock in the interference side of the two jets is distorted to the oblique shock owing to the strong interaction between the two jets. Again, a small reverse flow region exists upstream from the stagnation point on the symmetric axis, while there is an acceleration region of the jet gas downstream from the point and the Mach number exceeds unity. However, the gas velocity along the symmetric axis rapidly drops down due to the existence of a relatively strong normal shock.

At any rate, as mentioned above, the effect of the nozzle distance on the interaction of the two jets and the global structures of the interacting free jets will be demonstrated and discussed from an analytical point of view.

The present numerical experiments have been performed by a TVD (Total Variation Diminishing) scheme developed by Chakravarthy and Osher[13]. The calculation has been made on a Fujitsu VP-400E super computer at the Data Processing Center of Kyoto University. In passing, we note that the VP-rate in our computer program is approximately unity.

2. Governing equations

The jet is treated as a two-dimensional inviscid compressible flow. The system of equations governing flow fields is expressed by the following dimensionless variables;

$$
\left.
\begin{aligned}
&t = \frac{\bar{t}}{\bar{L}/\bar{c}_0}, \quad x = \frac{\bar{x}}{\bar{L}}, \quad y = \frac{\bar{y}}{\bar{L}}, \quad \rho = \frac{\bar{\rho}}{\bar{\rho}_0} \\
&p = \frac{\bar{p}}{\bar{p}_0}, \quad u = \frac{\bar{u}}{\bar{c}_0}, \quad v = \frac{\bar{v}}{\bar{c}_0}, \quad T = \frac{\bar{T}}{\bar{T}_0} \\
&c = \frac{\bar{c}}{\bar{c}_0}, \quad M = \sqrt{u^2 + v^2} \,/\, c
\end{aligned}
\right\} \quad (1)
$$

where t, x and y are the time, the distance along the symmetric axis (plane) between two nozzle centerlines and the vertical distance perpendicular to x-axis, respectively. ρ, p, u, v, T, c and M denote the density, the pressure, the velocity components in the x- and y-directions, the temperature, the sound speed and the Mach number, respectively. The subscripts 0 (zero) denote the reservoir condition, and the overbar denotes the dimensional quantities. $\bar{L}$ is a characteristic length of the flow system. We note here that the half height $\bar{H}/2$ at the nozzle exit is adopted as $\bar{L}$.

The basic equation governing a two-dimensional ideal gas flow is expressed in the vector form

$$\frac{\partial \boldsymbol{Q}}{\partial t} + \frac{\partial \boldsymbol{F}}{\partial x} + \frac{\partial \boldsymbol{G}}{\partial y} = 0 \tag{2}$$

in which

$$\boldsymbol{Q} = \begin{pmatrix} e \\ \rho \\ \rho u \\ \rho v \end{pmatrix}, \quad \boldsymbol{F} = \begin{pmatrix} (e+p/r)u \\ \rho u \\ \rho u^2 + p/r \\ \rho uv \end{pmatrix}, \quad \boldsymbol{G} = \begin{pmatrix} (e+p/r)v \\ \rho v \\ \rho uv \\ \rho v^2 + p/r \end{pmatrix} \tag{3}$$

in which e denotes the total energy per unit volume of the gas and is expressed as

$$e = \frac{p}{r(r-1)} + \frac{1}{2}\rho(u^2 + v^2) \tag{4}$$

Thus, pressure can be decoded from the dependent variables using

$$p = r(r-1)\left[e - \frac{(\rho u)^2 + (\rho v)^2}{2\rho} \right] \tag{5}$$

Here, r is the ratio of specific heats.

3.   Analytical procedure and computational conditions

The numerical scheme in the present work is the second-order accurate TVD scheme developed by Chakravarthy and Osher, which is commonly called the Osher scheme.

First, we wish briefly to consider the boundary condition adopted in the present calculation.   As Matsuda et al. have pointed out[14], because the Osher scheme does not include any explicit artifical viscosity to smear out unphysical disturbances, the numerical results are rather sensitive to the choice of the boundary conditions imposed on the numerical boundaries, which may produce or reflect unrealistic damage to the main flow.

The calculation of the single free jet is preliminarily performed in order to make it easy to compare the structures of the interacting jets with the case of the single jet. Figures 1(a) and 1(b) indicate the geometry of the computational domain for the single free jet (a) and the interacting jets (b), respectively.   The computations for the two cases can be performed on the half section on the basis of symmetry with respect to the x-axis.   For the single jet, the boundary AB corresponds to the half height ($=\bar{H}/2$) of the nozzle exit, while for the interacting jets, the boundary AB corresponds to the full height ($=\bar{H}$) of the nozzle exit.   The upstream boundary OA equivalent to

the half distance between the two nozzles is added. The other boundaries BC, CD and DE are identical for the two cases. That is to say, the ambient gas condition is
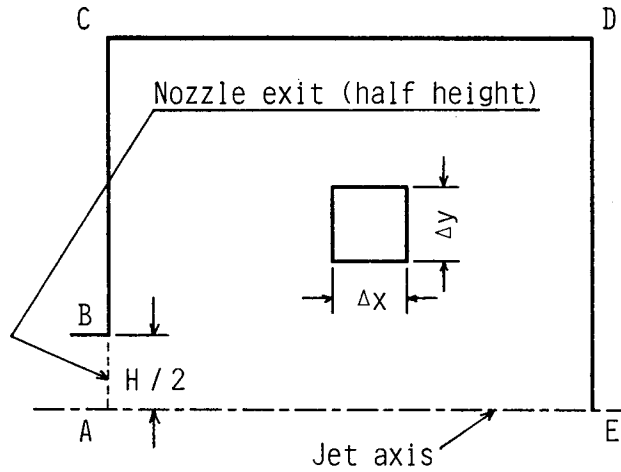
a) Single free jet
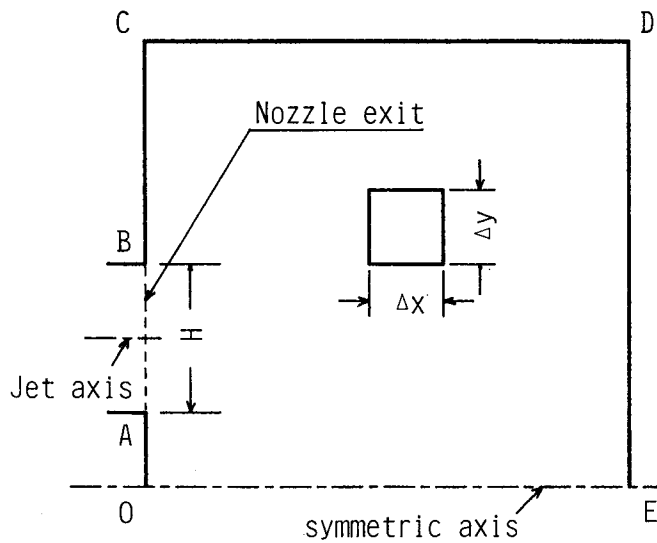
b) Interacting free jet

Figures 1(a) and 1(b) Geometry of computational domain for single free jet as well as interacting jets.

imposed on the upstream boundary BC (and OA also for the interacting jets case), the side boundary CD and the downstream boundary DE. The symmetric condition is applied to the symmetric axis AE for the single jet and OE for the interacting jets. Again, the jet condition is applied to the nozzle exit AB.

The physical variables are defined at the cell center in the cell method. Therefore, we must take two additional cells just outside the interior cell contacting with the boundary. This is because the fluxes just on the boundaries are calculated by solving a Riemann problem between the state in the additional cell and the state in the cell just inside of the boundary. When one calculates the physical variables in all the cells, including the additional cells, the specified boundary conditions are treated automatically, since the Riemann problems are solved at every cell and at every time step.

The Mach number of the jet at the nozzle exit is taken at $M_j = 1$, where the subscript, j, denotes the nozzle exit condition. The jet begins to blow at $t=0$ from a two-dimensional rectangular nozzle with $H=0.01$ m and a very large width. Also, it is assumed that a uniform ambient gas is at rest over the whole computational domain at $t=0$. In the present work, the ratio of $\bar{p}_0$ to $\bar{p}_\infty$ ($\bar{p}_0/\bar{p}_\infty$) is fixed to be 5.8, and the temperature ratio T_0/T_∞ is fixed to be unity where T_0 is the gas temperature in a reservoir. $\bar{p}_\infty$ and T_∞ denote the ambient gas pressure and temperature, respectively. $\bar{p}_\infty = 10^5$ [Pa] and $T_\infty = 300$ K are adopted throughout the present simulation. Again, the gas flow from the reservoir to the nozzle exit is assumed to be isentropic. Hence, the gas pressure at the nozzle exit is computed by the following formula assuming a quasi-one-dimensional flow;

$$\bar{p}_j = \bar{p}_0 \left[1 + \frac{\gamma - 1}{2} M_j^2 \right]^{-\gamma/(\gamma-1)} \tag{6}$$

Therefore, the condition that $M_j = 1$ gives the pressure ratio $\bar{p}_j/\bar{p}_0 = 0.528$ as $\gamma = 1.4$. That is, $\bar{p}_j/\bar{p}_\infty = 3.064$.

The computational space is different between the single jet and interacting jets cases. First, for the single jet, the computational space is $10H$ long along the jet axis and $2H$ long across it. Again, one should bear in mind that, as mentioned already, the computation is performed on the half section. The nozzle exit height H is arranged by 10 grid points. Note that $H/2$ is taken in this computation on the basis of the symmetry with respect to x-axis (see Figure 1(a)). Therefore, the number of meshes involved in the computational domain is taken at 100×20.

Second, for the twin (or interacting) jets, the computational space is $10H$ long along the symmetric axis and $5H$ long across it. In this case, the number of meshes

involved in the computational domain is taken at 100×50.

Next, denoting the mesh sizes by Δx and Δy, the integration time step Δt obeys

$$\Delta t = F \cdot \text{Min} \left\{ \frac{\text{Min}(\Delta x, \Delta y)}{c + \sqrt{u^2 + v^2}} \right\} \tag{12}$$

in which F is an appropriate constant less than unity. In the present calculation, $F=0.4$ has been selected. Again, $\Delta x = \Delta y = 0.2$.

In addition, the present numerical scheme is coded so that the program may be applicable to the calculations of various flow fields; flows around solid objects such as wedges, flat plates, cavities, spheres etc., axisymmetric free jet flows and so on. We have preliminarily checked whether the scheme is valid or not, specifically for the calculations of flow structures of axisymmetric free jets. The numerical results so obtained have been compared with the experimental ones by Love et al.[15]. We note that the agreement between the numerical and experimental results is excellent. The details are explained in our previous paper[16].

4. Numerical results and discussion

4.1 Single free jet

We first present the calculated results of the single free jet. Figures 2(a) to 2(e) indicate the variations of the density contours for the free jet expanded into a stagnant ambient gas with the time step where N is the number of computationsl time step. Here, we note that the density contours are shown at 20 equal linear intervals between the maximum density and the minimum one throughout the present paper, unless otherwise stated. At $N=1000$, the configuration of the first shock cell has been completed, but that of the second cell has not been built up. After $N \gtrsim 2000$, the quasi-steady or quasi-converged stage is reached and the two shock cells whose configuration and size are almost similar to each other have been established, although we cut down the downstream part of the second shock cell due to the influence of the downstream boundary condition.

Figures 3(a) to 3(e) show the velocity vector fields at the corresponding time steps. These figures profile the configuration of the cell structures presented by the above density contours. This calculation was continued up to $N=5000$, and the state of the flow field over $N=2000$ appears to be very stable, as mentioned already.

Figures 4(a) to 4(e) indicate the distributions of the pressure contours at the time steps corresponding to those shown in Figures 2(a) to 2(e). At the expansion part of the nozzle exit and at the rear edge of the first shock cell (as well as the frontal edge of
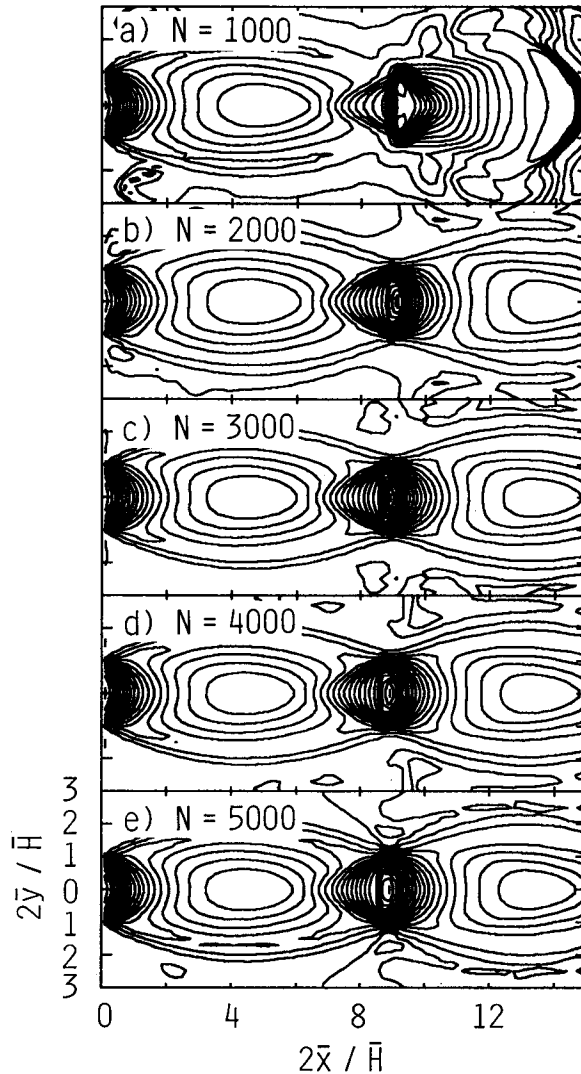
Figures 2(a) to 2(e)   Variation of density contours for single free jet with time step N.

the second shock cell), the pressure gradient (the density gradient as well) is seen to be very steep.   That is, the gas flow at the nozzle exit emanates successively and stably the expansion waves to the downstream region.   Then the gas pressure reaches an overexpansion state in the central region of the first shock cell.   Next, the compression waves begin to govern the gas flow down the jet stream.   As a result, the gas pressure attains a peak at the rear edge of the first shock cell.   The pressure contours are closed in the form of a loop between the rear edge of the first shock cell and the frontal
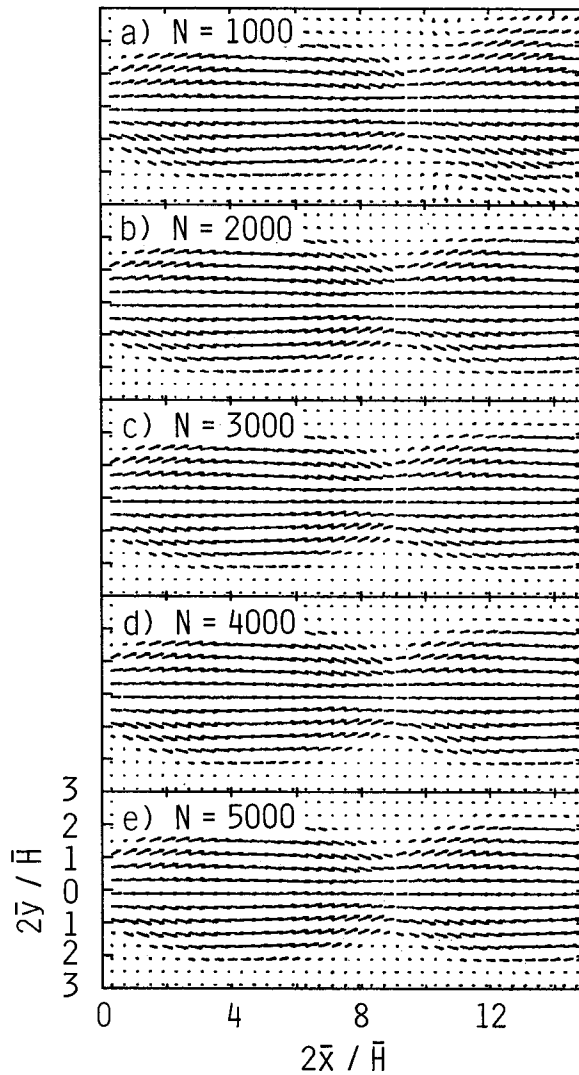
Figures 3(a) to 3(e)   Velocity vector fields at various time steps.

edge of the second cell.   Then, the highest pressure gas at the frontal edge of the second cell (or the rear edge of the first one) expands downstream to the central part of the second cell, and reaches the minimum in the central part of the second cell, as seen in the first shock cell.

Figures 5(a) to 5(e) give the distribution of the temperature contours at the corresponding time steps.   The temperature gradient along the jet axis is seen to be not so steep even at the nozzle exit and the boundary between the two cells.   Rather, the
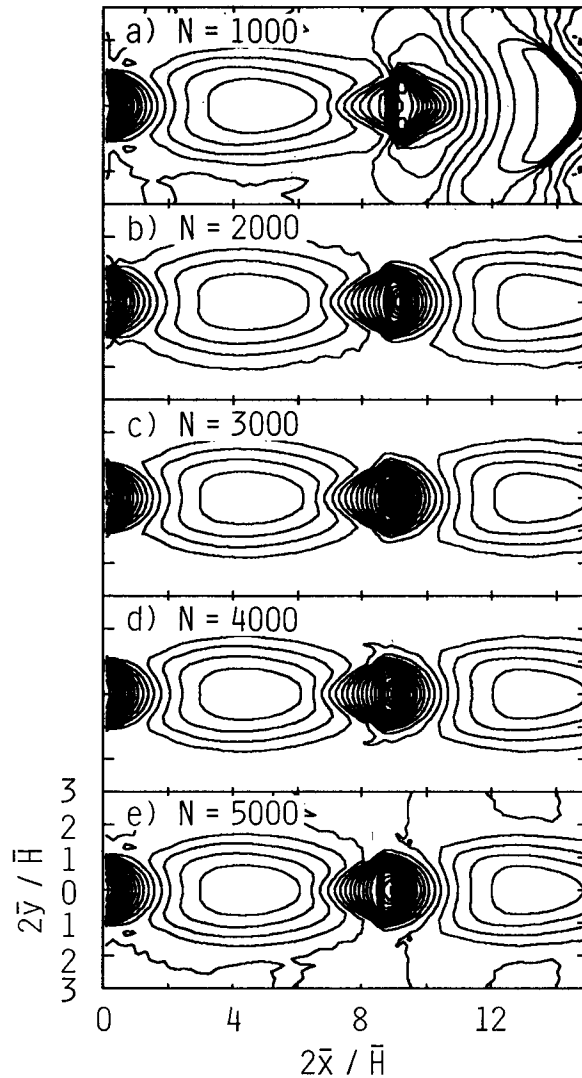
Figures 4(a) to 4(e)   Distributions of pressure contours at various time steps.

temperature gradient in the direction perpendicular to the jet flow becomes violent at the jet boundaries.

Figures 6(a) to 6(c) give the distribution of the density (a), pressure (b) and Mach number (c) along the jet axis at N=3000, 4000 and 5000.   According to the present numerical results, the expansion region of the first shock cell is understood to be time-independent, but the time-independent or time-converged numerical solution in the downstream region is seen to be unobtainable in a perfect sense, although this fluctua-
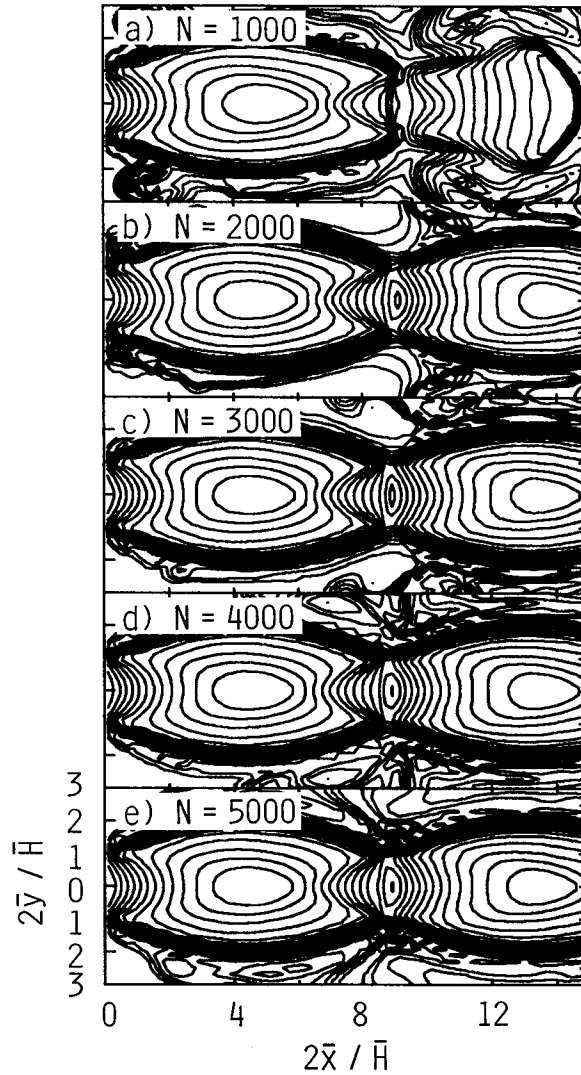
Figures 5(a) to 5(e)   Distributions of temperature contours at corresponding time
steps.

tion is very slight.   A visual comparison between an instantaneous photograph and a
long-time-exposure one has been performed in the analysis of choked underexpanded
jets[14].   The result exhibits that the flow in the instantaneous photograph fluctuates
very much while the long-time-exposure photograph shows a rather smooth and regu-
lar pattern.   It can be pointed out that the latter corresponds to the time-averaged
flow of the former.   This also supports the slightly fluctuating behaviour of the pre-
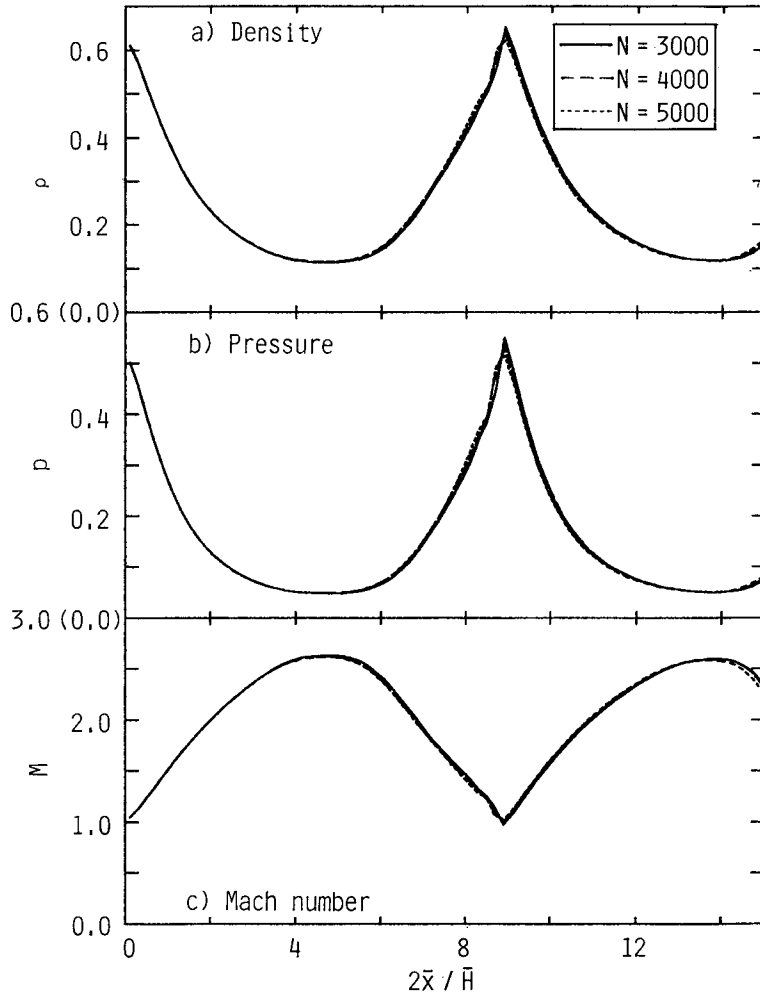
Figures 6(a) to 6(e)   Profiles of density (a), pressure (b) and Mach number (c) along
jet axis at N=3000, 4000 and 5000.

sent simulations.

Figure 7 indicates the time-averaged profiles of the pressure, the density and the temperature along the jet axis where these values are averaged over 1000 time-steps from N=4001 to 5000.   The length of the first shock cell structure is about 4.5 times of the nozzle height.   As can be expected, both the upstream and downstream parts of the cell structure always take the high pressure, high density and low Mach number, while the central part always takes the minimum pressure and density, but the maximum Mach number, as mentioned already.   One of the prominent features is that
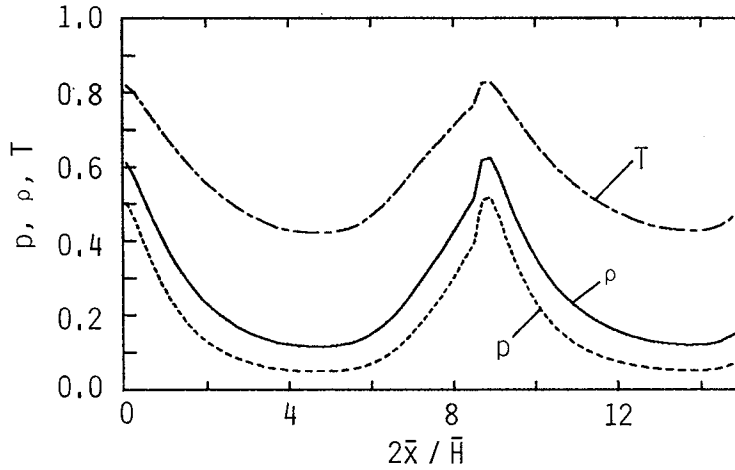
Figure 7   Time-averaged profiles of pressure, density and temperature along jet axis.   Note that these values are averaged over 1000 time-steps from N= 4001 to 5000.

no Mach disk is observed regardless of a relatively high ratio of p_j to p_∞.

Figures 8(a) to 8(e) give the numerical results of the distributions of the vorticity ζ ($=\partial v/\partial x-\partial u/\partial y$) at N=1000, 2000, 3000, 4000 and 5000.   It follows from the present calculation that the distribution of the vorticity is arranged along jet boundaries due to the velocity difference between the jet core and the ambient gas.   The vorticity with the largest value exists just at the nozzle exit.

4.2   Interacting free jets

Two cases where the distances between the centerlines of nozzles is $2\bar{H}$ and $3\bar{H}$ are simulated.   The former will be called simply the $2\bar{H}$ case, hereafter, and the latter the $3\bar{H}$ case.

Figures 9(a) and 9(b) indicate the variations of the density contours with time as well as the comparison between the $2\bar{H}$ case (a) and the $3\bar{H}$ case (b) at the same computational time steps.   It can be understood that the interior structure of the interacting jets is different between the two cases at a few aspects.   First, for the $2\bar{H}$ case, the point where the two jets interact with each other is seen to approach the fairly upstream side on the symmetric axis in comparison with the $3\bar{H}$ case.   While for the $3\bar{H}$ case, the interacting point exists on the downstream side, and therefore the first shock cell structure similar to that of the single free jet is going to be formed at N= 1000.   Second, the establishment of some relatively stable shock waves is fairly clearly recognized in the $2\bar{H}$ case already at N=1000, and a normal shock wave is distinctly
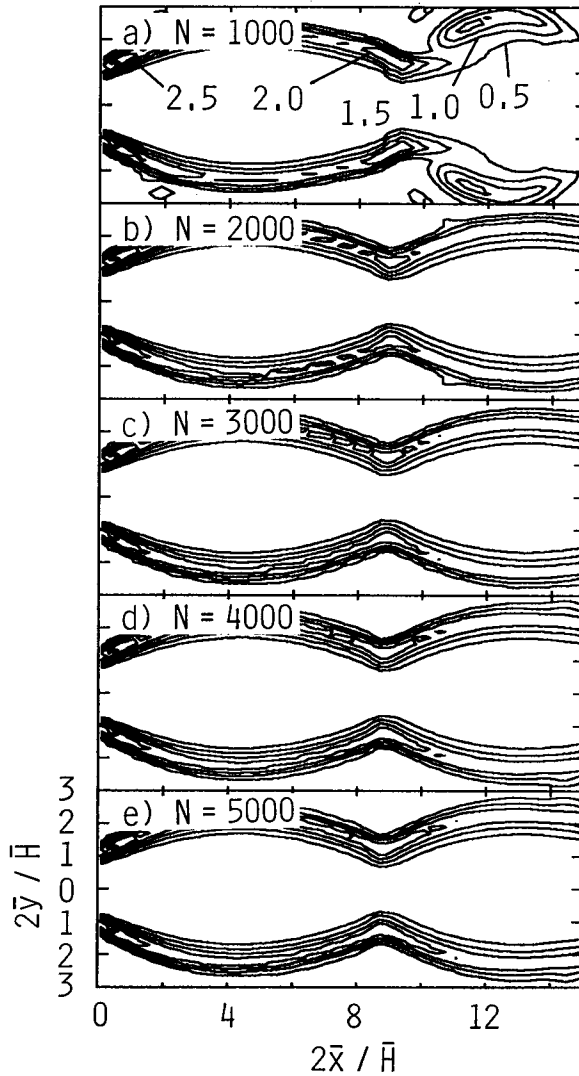
Figures 8(a) to 8(e)   Distributions of vorticity, ζ $(=\partial v/\partial x - \partial u/\partial y)$, at various time steps.

seen to be formed in the direction perpendicular to the symmetric axis. Therefore, the gas velocity (or Mach number) along the symmetric axis rapidly drops down at $x(=2\bar{x}/\bar{H})=8.5$ or so, as will be shown later. However, in the $3\bar{H}$ case, such normal and oblique shock waves can be seen neither along symmetric axis nor along the nozzle axis.

Figures 10(a) and 10(b) indicate the variations of the velocity vector fields of the

$2H$ and $3H$ cases with time at the same computational time steps. For the $2H$ case, comparing this with the corresponding density contours shown in Figure 9(a), it is possible to find where the shock waves are present in the flow field. First of all, it is noticeable that the point of the interaction between the two jets corresponds to the stagnation point and is located fairly upstream along the symmetric axis. A small reverse flow region is observable upstream from the point. On the contrary, downstream from the stagnation point, there exists an acceleration of the jet gas along the symmetric axis. However, as mentioned above, it can be seen that the gas velocity rapidly drops down through a shock normal to the symmetric axis. In addition, some oblique shock waves in the flow field can be confirmed on the basis of both the magnitude and the direction of the velocity vectors. Next, for the $3H$ case, it can be seen that the gas velocity in the region between the two jets is stagnantly small and the interacting point corresponding to the stagnation point exists on the fairly downstream side at $x\simeq11.5$. Again, a reverse flow along the symmetric axis occurs upstream from the stagnation point and thereby a circulating flow is formed in a relatively wide region between the two jets. Also, it is interesting to note that the profile of the first shock cell similar to that of the single jet is observable in a clear form, but the profile of the second shock cell is deformed by the strong interaction between the two jets.

Figures 11(a) and 11(b) indicate the variations of the pressure contours with time as well as the comparison between the $2H$ case (a) and the $3H$ case (b) at the same time steps as shown in the previous figures. The configurations of the pressure contours are very similar to those of the density contours concerning the expansion waves at the nozzle exit, the multiple loops expressing the steep pressure gradient at the rear edge of the first shock cell and the arrangement of shock waves (for the $2H$ case).

Figures 12(a) and 12(b) give the variations of the temperature contours with time as well as the comparison between the $2H$ and $3H$ cases at the corresponding time steps. The temperature gradient is steep at the jet boundaries. The result is similar to the single jet case (see Figures 5(a) to 5(e)). This fact is considered to be due to the temperature difference between the gas flowing in the shock cell and the ambient gas. The former is lower than the latter. The gas temperature at the nozzle exit is that $T_j=0.833\ T_\infty\ (T_0=T_\infty)$. This temperature drops further due to the expansion. Also, when the distance between the centerlines of the nozzles is taken to be small, the rapid change in temperature is observable at the shock wave.
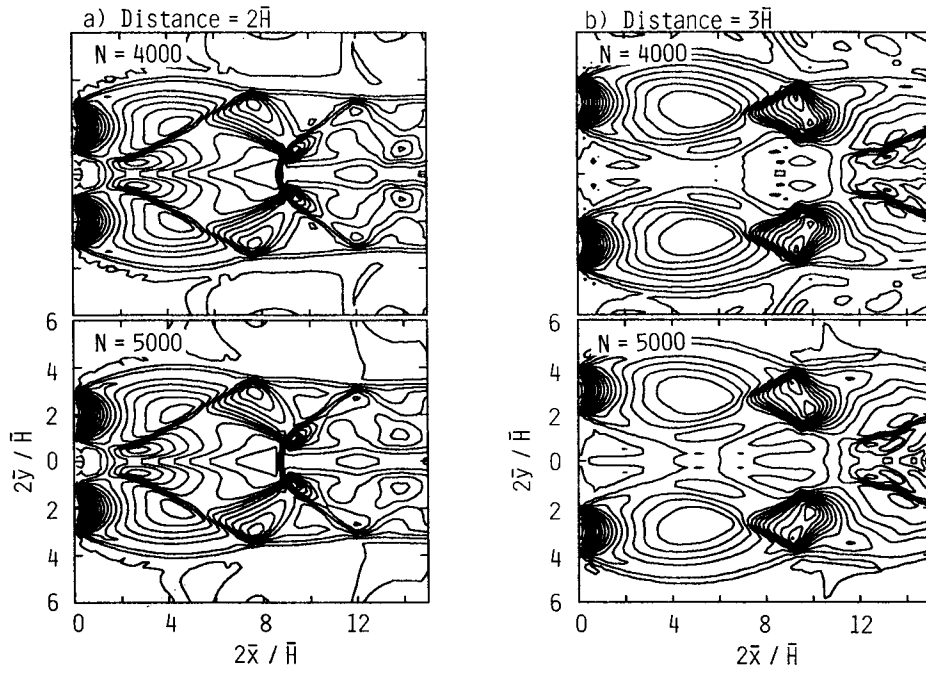
Next, we consider the flow properties both along the symmetric axis and along the jet axis (equivalent to the nozzle centerline).

Figures 13(a) and 13(b) indicate the time history of the Mach number along the symmetric axis (a) and the jet axis (b) for the $2H$ case. This is taken at five intervals

a) Distance = 2H̄

N = 1000

N = 2000

N = 3000

b) Distance = 3H̄

N = 1000

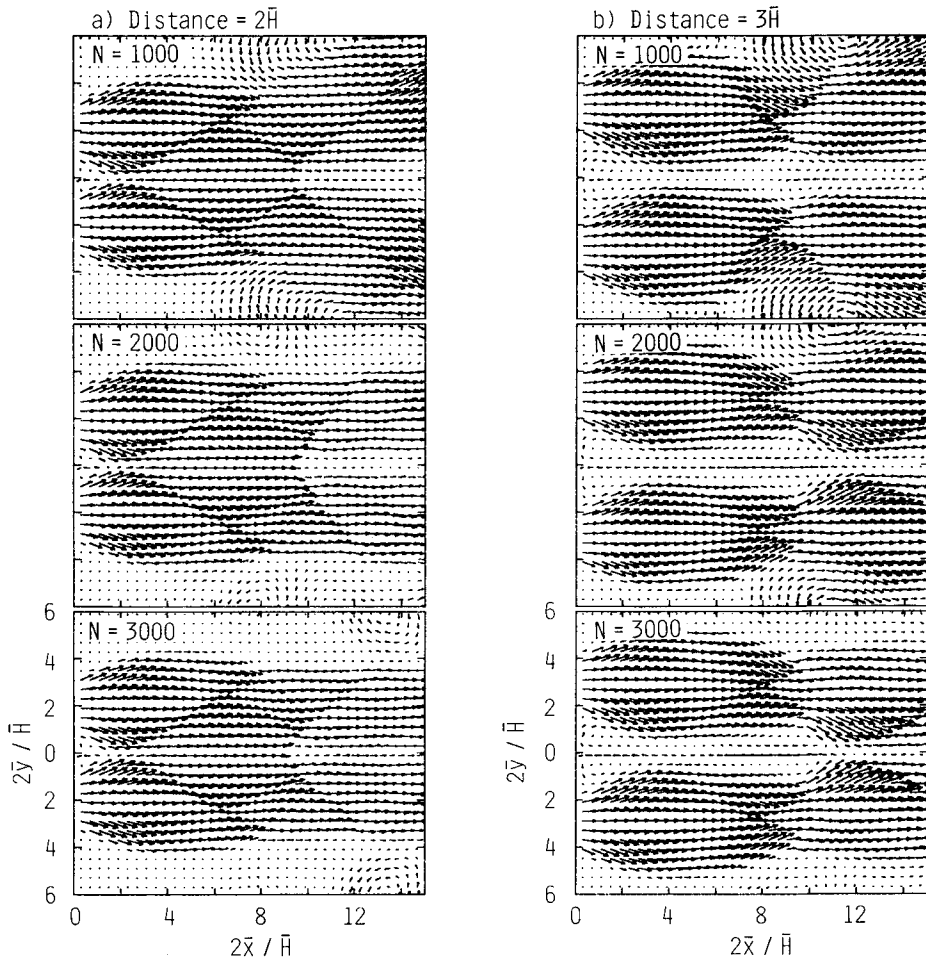N = 2000

N = 3000

2ȳ / H̄

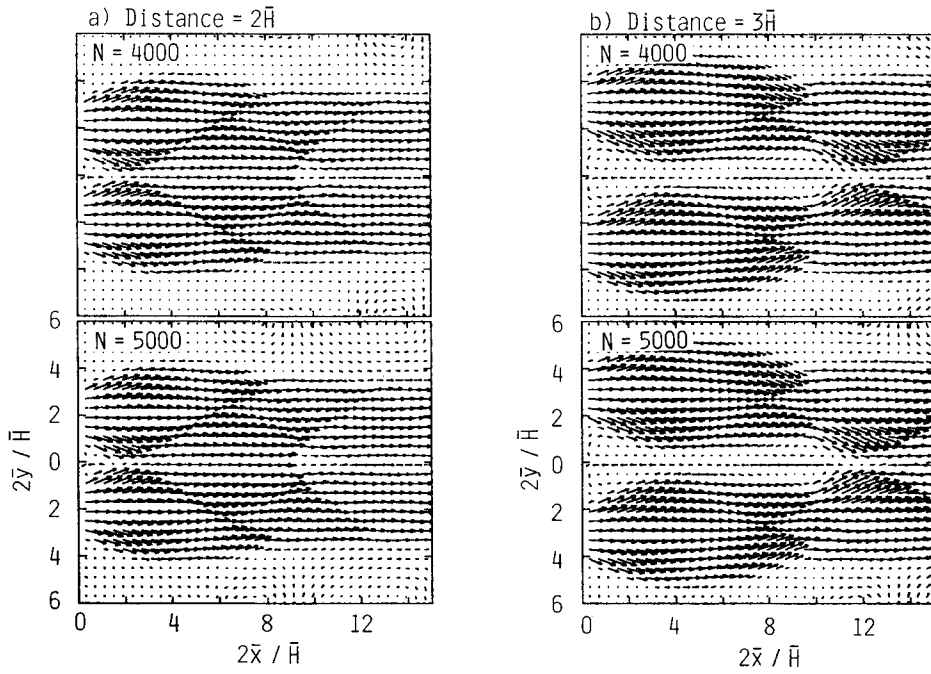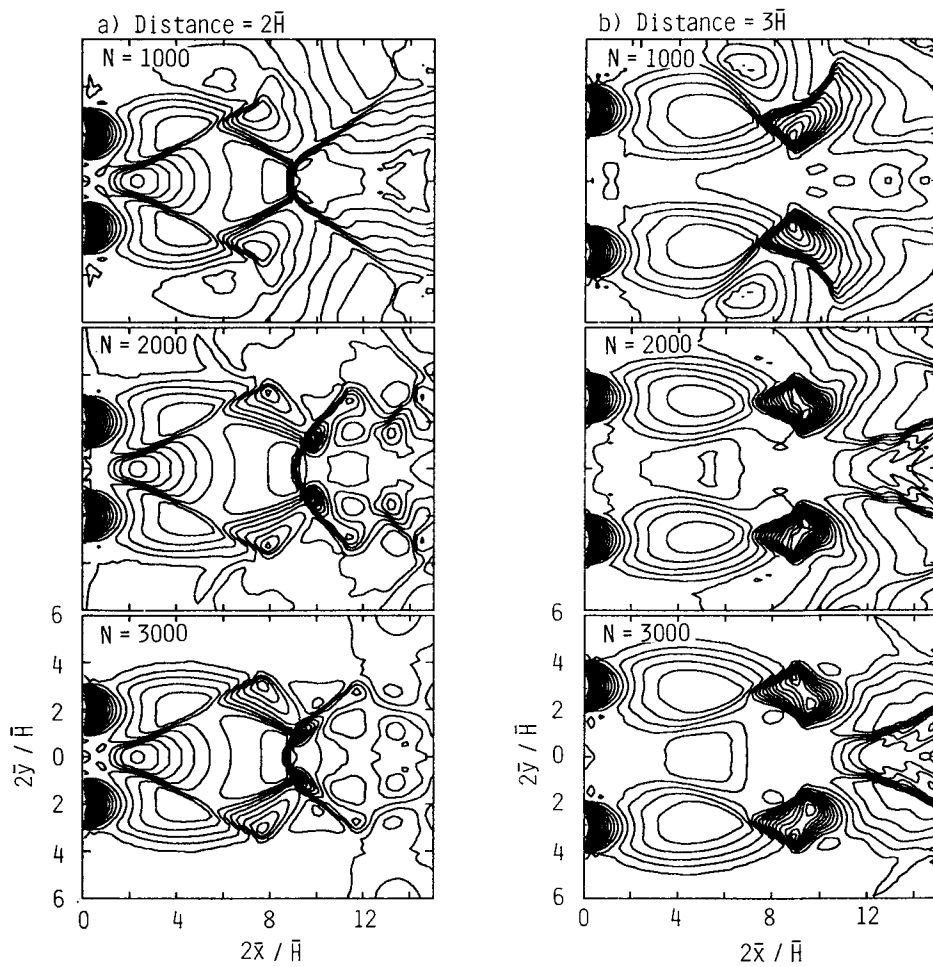2x̄ / H̄
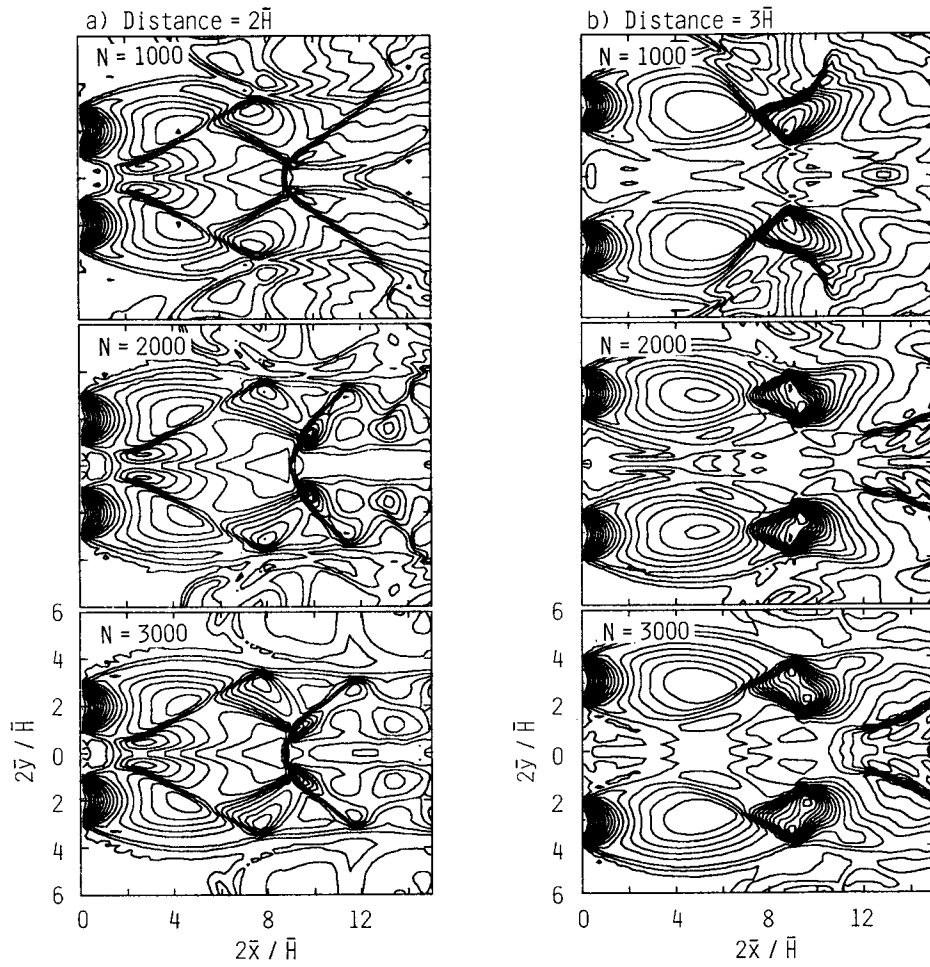
Figures 9   For caption see next page.

Figures 9(a) and 9(b)   Variation of density contours with time as well as comparison
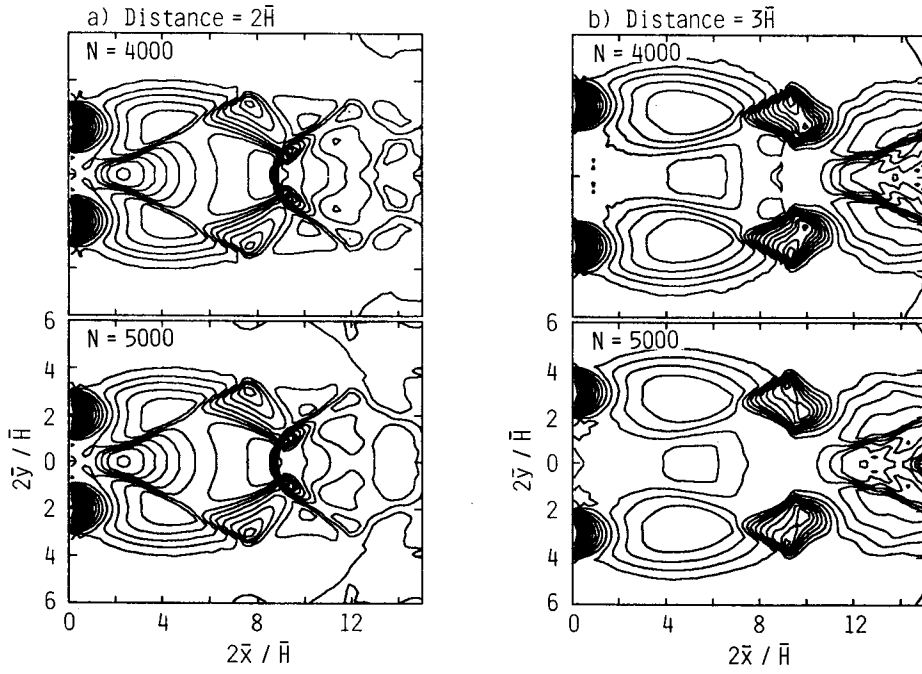$2\bar{H}$ case (a) and $3\bar{H}$ case (b) at various time steps.

a) Distance = 2H̄

b) Distance = 3H̄

Figures 10   For caption see next page.

Figures 10(a)and 10(b)   Variation of velocity vector fields of the $2\bar{H}$ (a) and $3\bar{H}$ (b) cases with time, as well as comparison between two cases at the same computational time steps.
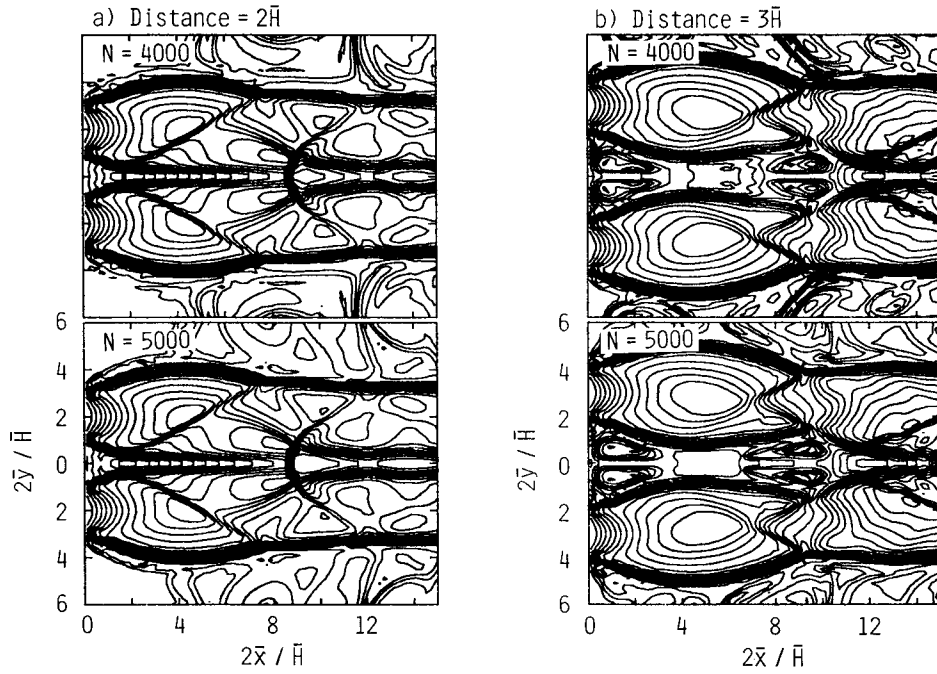
Figures 11   For caption see next page.

Figures 11(a) and 11(b)   Variation of pressure contours with time as well as comparison between $2\bar{H}$ case (a) and $3\bar{H}$ case at the time steps.

a) Distance = 2H̄

b) Distance = 3H̄
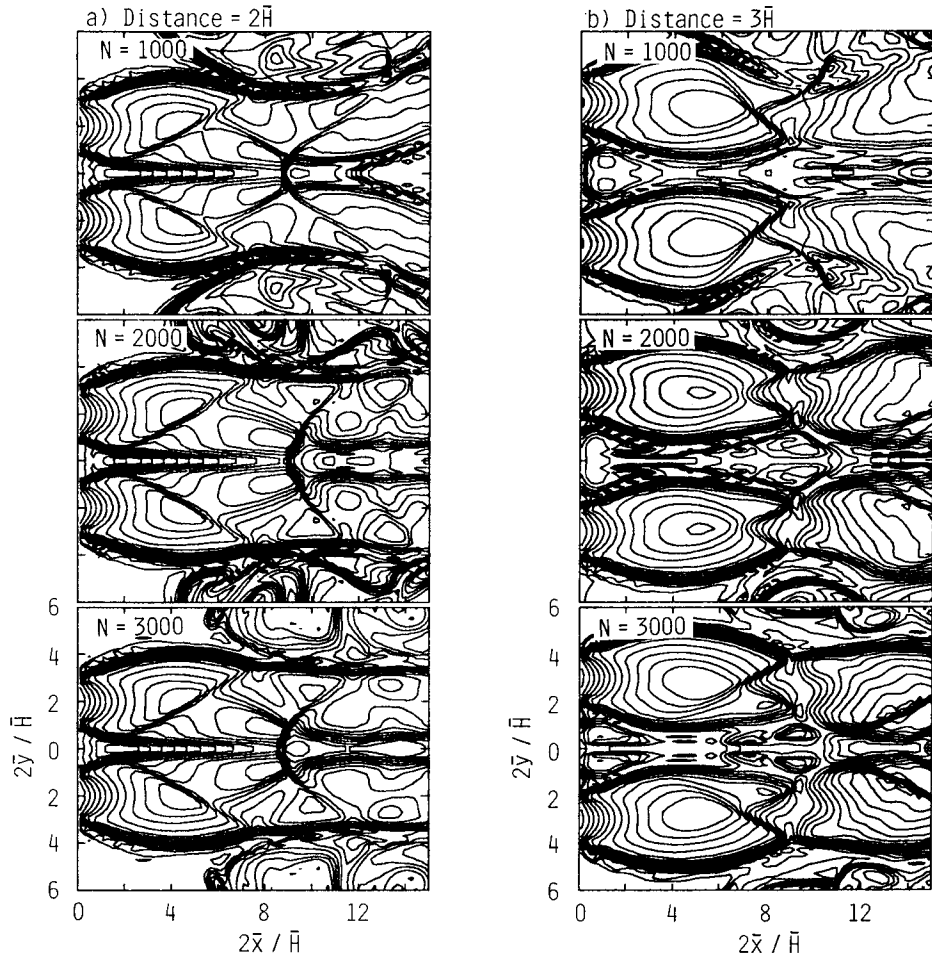
Figures 12   For caption see next page.

a) Distance = 2$\bar{H}$

b) Distance = 3$\bar{H}$

Figures 12(a) and 12(b)   Variation of temperature contours with time as well as comparison between 2$\bar{H}$ (a) and 3$\bar{H}$ cases at the same time steps.

a) Symmetric axis   b) Jet axis
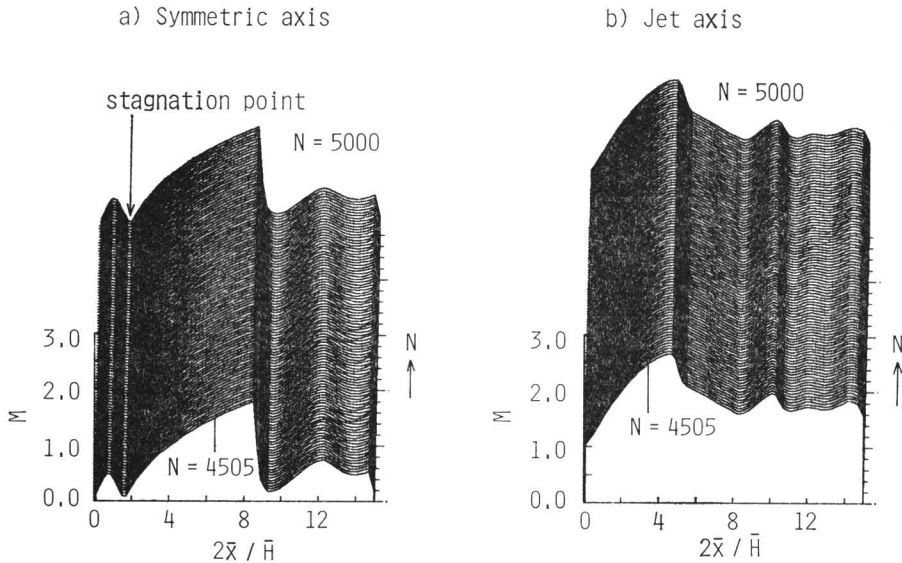
Figures 13(a) and 13(b)   Time history of Mach number along symmetric axis (a) and
along jet axis (b) for $2\bar{H}$ case. Note that the numerical
results are taken at five intervals from N=4505 to 5000.

from N=4505 to N=5000. The jet expands very sharply near the nozzle exit, and
therefore the Mach number increases to $M \simeq 2.7$ at $x \simeq 4.2$ along the jet axis. As
mentioned already, a stagnation point exists on the fairly upstream side ($x \simeq 1.8$) along
the symmetric axis, and downstream from the point, the Mach number grows in a
smooth state and exceeds unity ($M \simeq 1.8$). However, at $x \simeq 8.5$ the Mach number
rapidly drops down owing to the appearance of the shock normal to the symmetric
axis. Obviously, the pressure jump must occur at this point, as will be shown later.
Again, the gas flows reversely upstream from the stagnation point along the symmetric
axis (refer to Figure 10 (a)).

Figures 14(a) and 14(b) give the time history of the Mach number for the $3\bar{H}$
case, corresponding to the $2\bar{H}$ case shown in Figures 13(a) and 13(b). The distribu-
tions of the Mach number along the jet axis are similar to those of the single free jet.
Both ends of the shock cell take the low Mach number, while the central part of the
cell takes the high Mach number. However, such a fluctuating tendency seems to
have some irregularity downstream along the nozzle centerline. Also, the Mach
number along $y=0$ is always below unity. At $x \simeq 11.5$, the jet gas stagnates, and the
gas flows reversely from the point to the upstream side along $y=0$ (see Figures 10(b)).

In fact, we note that the gas fluctuates downstream in the interaction region for
both the $2\bar{H}$ and $3\bar{H}$ cases. That is, a time-converged solution, in the conventional
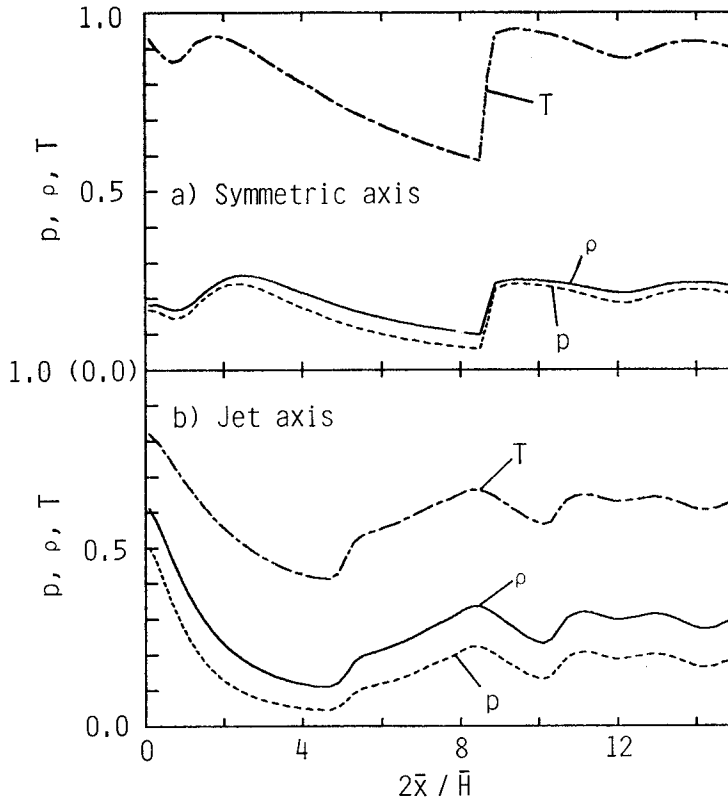
a) Symmetric axis   b) Jet axis
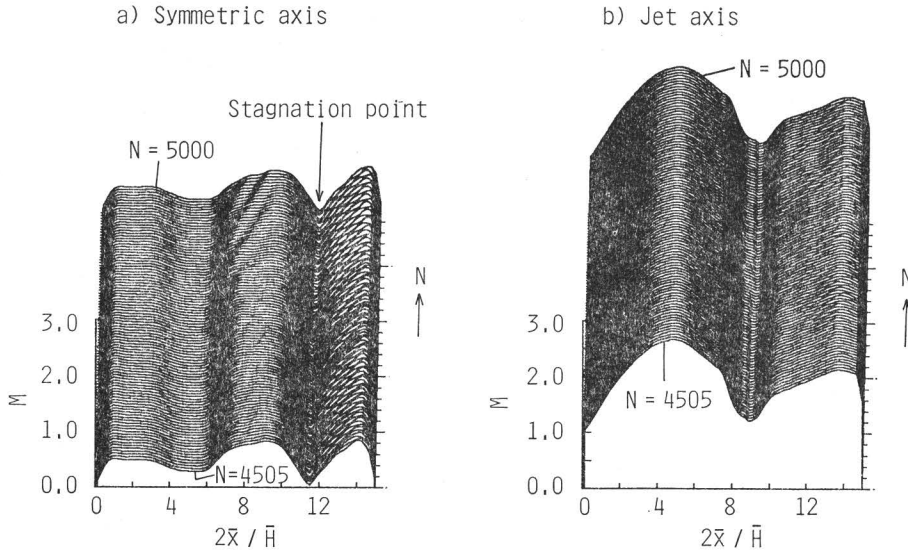
Figures 14(b) and 14(b)   Time history of Mach number for $3\bar{H}$ case, corresponding to $2\bar{H}$ case shown in the above figures.

sense, has not been reached at all, even at N→∞.

Figures 15(a) and 15(b) are the time averaged pressure, density and temperature over 500 time steps from N=4501 to N=5000 along the symmetric axis (a) and the jet axis (b) for the $2\bar{H}$ case. The three flow properties take a slight peak on the fairly upstream side (at $x\simeq2$) along the symmetric axis ($y=0$), and then drop down in a smooth state from this point to $x\simeq8.5$. Next, the pressure, density and temperature jumps are obviously observed to occur at $x\simeq8.5$ due to the existence of the shock normal to the symmetric axis. For the variations of the flow properties along the jet axis ($y=2$), p, ρ and T are all decreased to an appreciable degree by the expansion of the gas at the nozzle exit, and then increased due to the appearance of the oblique shock wave. Again, the gas meets a different oblique shock wave after the compression and expansion. The three flow properties change according to such circumstances along the jet axis.
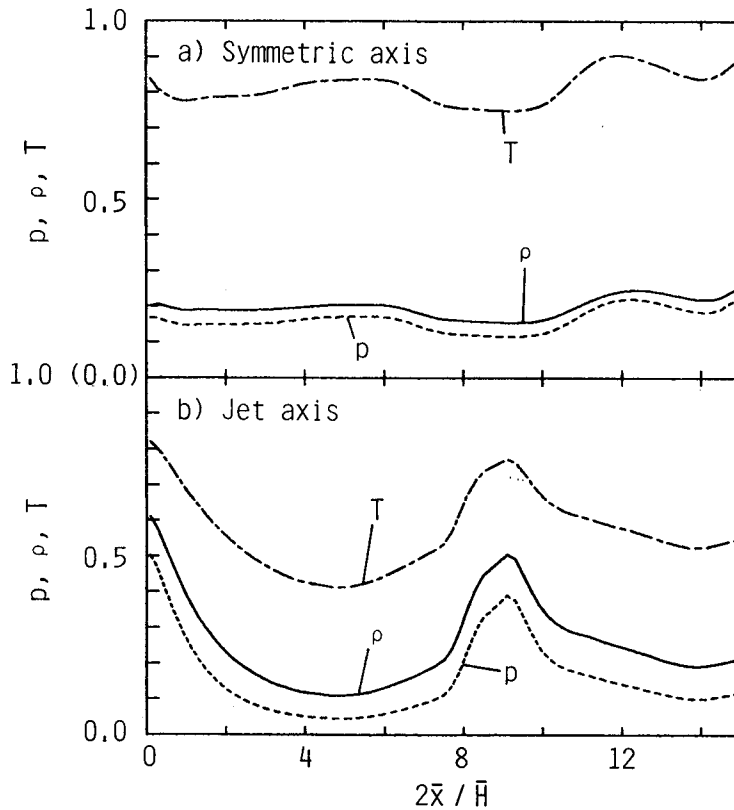
Figures 16(a) and 16(b) display the numerical results for the $3\bar{H}$ case, corresponding to Figures 15(a) and (b). There are no remarkable changes in the flow properties along the symmetric axis, because no discontinuity waves (shock waves) exist along the symmetric axis, as shown in Figure 9(b). Next along the jet axis, the gas flow at the nozzle exit emanates successively and stably the expansion waves to the downstream region, and then the gas pressure reaches an overexpansion state in the central region of the first shock cell. After that, the compression waves govern the gas flow.

Figures 15(a) and 15(b)   Time-averaged pressure, density and temperature over 500
time-steps from N=4501 to 5000 along symmetric axis (a)
and along jet axis (b) for $2\bar{H}$ case.

Such changing behaviours of the flow properties along the jet axis are found to be roughly similar to the results of the single jet (compare these with Figures 6 (a) and 6 (b)), but the effect of the interaction between the two jets is seen to appear for the downstream region corresponding to the second shock cell.

Figures 17(a) and 17(b) give the variations of the vorticity distributions with time as well as the comparison between the $2\bar{H}$ case (a) and the $3\bar{H}$ case (b) at every 1000 time steps from N=1000 to 5000. From these figures and Figures 10(a) and (b), the presence of the vortical structure is well observed at the outer jet boundaries (on the free side). The magnitude of the vorticity is basically similar for the two cases and takes the maximum value just at the nozzle exit. However, the configuration of the vorticity contours at the inner jet boundaries (on the interference side) is different for the two.

Figures 16(a) and 16(b)   Numerical results for $3\bar{H}$ case, corresponding to the above figure.

5. Concluding remarks

The Euler equation has been solved to obtain the time dependent flow patterns of choked underexpanded jets using the second-order explicit Osher scheme in a two-dimensional Cartesian coordinate system.   The computational results have been demonstrated for the two cases.

First, a choked underexpanded supersonic single free jet has been investigated in detail in the context of continuum ideal gas dynamics.   This has been performed in order to compare the flow structures of a single free jet with those of two interacting free jets.   It is worthwhile to mention that the first shock cell structure in the neighbourhood of the nozzle exit is formed fairly in an earlier stage of the evolution (at N $\simeq 1000$) and its global structure does not change with time.   After that, the second cell is formed successively.   However, even for single free jets, a slightly oscillatory
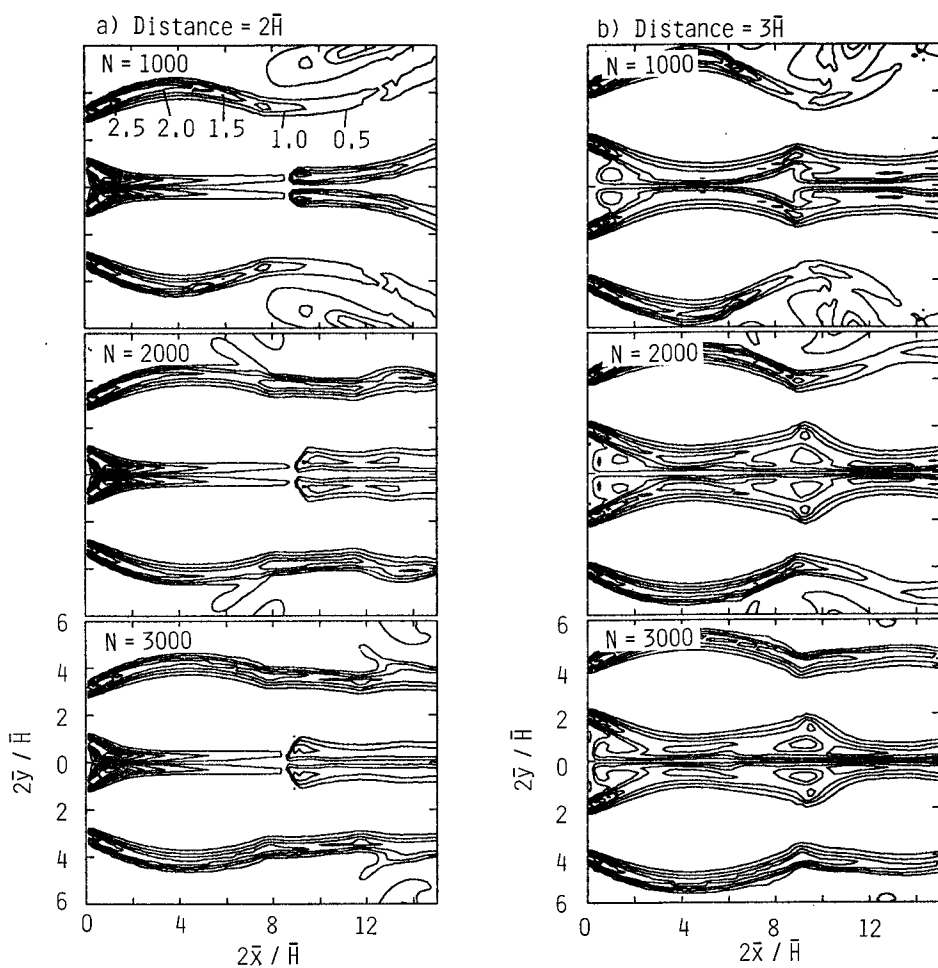
Figures 17   For caption see next page.

motion is seen to occur at the frontal edge of this cell.

Second, the structures of the interacting free jets expanded from two parallel sonic nozzles have been numerically analyzed.   These jets are all the same as the above case.   Here, two kinds have been treated where the distances between the centerlines of the nozzles are taken at $2H$ and $3H$ (H; nozzle height at the exit).

It has been shown that the configuration of shock cell structures, as encountered in the single free jet, can be observed nowhere owing to the strong interaction of the two jets, when the distance between the nozzle centerlines is kept at $2H$.   Again, the interacting point of the two jets corresponding to the stagnation point approaches the considerably upstream side along the symmetric axis in comparison with the case of
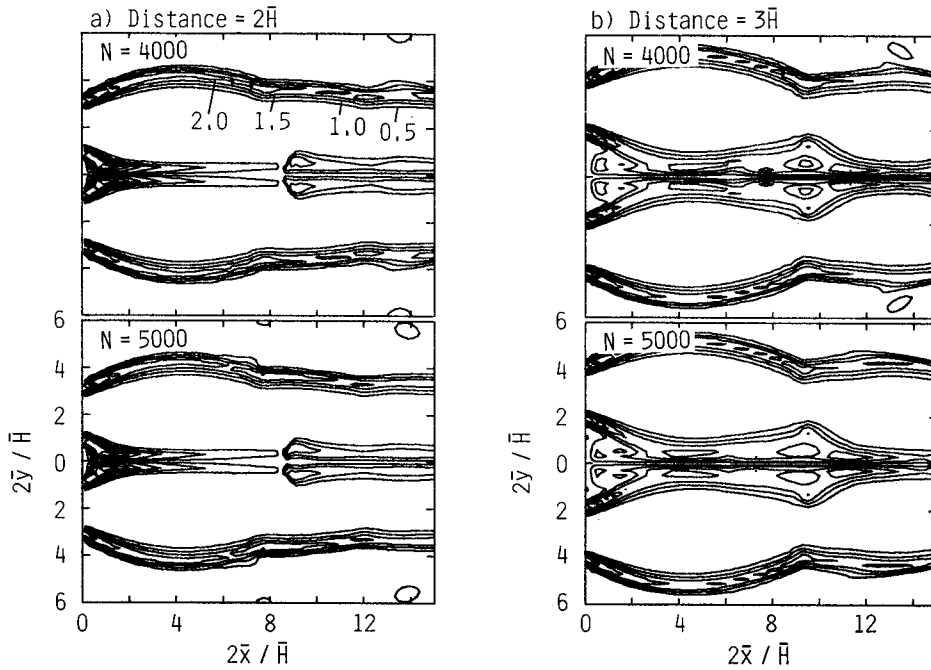
Figures 17(a) and 17(b) Variation of vorticity distributions with time as well as comparison between $2\bar{H}$ (a) and $3\bar{H}$ (b) cases at the same time steps.

the large nozzle distance.   Furthermore, the Mach number along the jet axis is always kept beyond unity, and the shock normal to the symmetric axis stands at $\bar{x}\simeq4.2\bar{H}$. Therefore, the numerical solution is not time-converged in the exact sense, but rather oscillatory, particularly in the downstream region.

Next, when the nozzle distance is kept at $3\bar{H}$, the interacting point of the two jets is located at the relatively downstream side.   Therefore, the shock cell structure similar to that of the single free jet is formed upstream from the point owing to the weak interaction of the two free jets, and the existence of the barrel shock is confirmed along the shock cell boundaries.   Also, we have found that circulating flows exist in a relatively wide region between two first shock cells.   Although the degree of the interaction in the $3\bar{H}$ case is much weaker than in the $2\bar{H}$ case, the numerical solution is slightly oscillatory in the downstream region.

References

1) Hatta, N., Ishii, R., Takuda, H., Ueda, K., and Kokado, J., "Analytical Study on Subsonic Nozzle Flows of Gas-Particle Mixture, "Trans. Iron Steel Inst. Jpn., Volume 28, July 1988, pp. 930–938.

2) Hatta, N., Takuda, H., Ishii, R., and Fujimoto, H., "A Theoretical Study on Nozzle Design for Gas-Particle Mixture Flow," ISIJ International, Volume 29, July 1989, pp. 605–613.

3) Hatta, N., Fujimoto, H., Ishii, R., Umeda, Y., and Kokado, J., "Numerical Study on Supersonic Flows of Gas-Liquid Particle Mixture in a De Laval Nozzle," ISIJ International, Volume 29, November 1989, pp. 911–918.

4) Harlow, F. H., and Amsden, A. A., "Numerical Calculation of Multiphase Fluid Flow," Journal of Comput. Physics, Volume 17, 1975, pp. 19–52.

5) Hatta, N., Ishii, R., and Fujimoto, H, "Impingement of Two-Phase Subsonic Jets on a Flat Plate," submitted to the ASME Journal of Fluids Engineering, 1990.

6) Ishii, R., Umeda, Y., and Yuhi, M., "Numerical Analysis of Gas-Particle Two-Phase Flows," J. Fluid Mechanics, Volume 203, pp. 475–515.

7) Ishimaru, S., and Nishida, M., "Numerical Analysis of Gas-Solid Two-Phase Supersonic Freejets," Trans. JSME ((B), in Japanese), Volume 55, August 1989, pp. 2262–2267.

8) Hatta, N., Fujimoto, H., Ishii, R., and Kokado, J., "Analytical Study of Gas-Particle Two-Phase Free Jets Exhausted from a Subsonic Nozzle," ISIJ International, Volume 31, January 1991, pp. 53–61.

9) Hatta, N., Ishii, R., and Fujimoto, H., "Gas-Particle Two-Phase Subsonic Freejets," submitted to the ASME Journal of Fluids Engineering, 1990.

10) Fujimoto, T., Niimi, T., and Osada, H., "A Study on Interacting Free Jets," Trans. JSME ((B), in Japanese), Volume 53, February 1987, pp. 400–407.

11) Fujimoto, T., Niimi, T., and Osada, H., "A Study on Interacting Free Jets (2nd Report, 3-Dimensional Structure of Shock Systems)," Trans. JSME ((B), in Japanese), Volume 53, August 1987, pp. 2377–2383.

12) Fujimoto, T., Niimi, T., Osada, H., and Shimizu, H., "A Study on Interacting Free Jets (3rd Report, Structures of Interacting Free Jets with Different Source Pressure), Trans. ISME ((B), in Japanese), Volume 55, August 1989, pp. 2268–2275.

13) Chakravarthy, S. R., and Osher, S., "A New Class of High Accuracy TVD Schemes for Hyperbolic Conservation Laws," AIAA 85-0363, AIAA 23rd Aerospace Science Meeting, January 1985/Reno, Nevada.

14) Matsuda, T., Umeda, Y., Ishii, R., Yasuda, A., and Sawada, K., "Numerical and Experimental Studies on Choked Underexpanded Jets," Mem. Faculty of Engineering, Kyoto University, Volume 48, 1987, pp. 84–110.

15) Love, E. S., Grigsby, C. E., Lee, L. P., and Woodling, M. J., "Experimental and Theoretical Studies of Axisymmetric Free Jets," NASA Technical Report R-6, 1959.

16) Hatta, N., Fujimoto, H., Ishii, R., and Kokado, J., "Theoretical Analysis of Supersonic Gas-Particle Two-Phase Flow and Its Application to Relatively Complicated Flow Fields," Mem. Faculty of Engineering, Kyoto University, Volume 52, Part 3 October 1990, pp. 115–185.